Continuum modelling of pantographic sheets for out-of-plane bifurcation and vibrational analysis

I. Giorgio, N. L. Rizzi, E. Turco

Continuum modelling of pantographic sheets for out-of-plane bifurcation and vibrational analysis

Giorgio, I. and Rizzi, N. L. and Turco, E.

Abstract

A nonlinear 2D continuum with a latent internal structure is introduced as a coarse model of a plane network of beams which, in turn, is assumed as a model of a pantographic structure made up by two families of equispaced beams, superimposed and connected by pivots. The deformation measures of the beams of the network and that of the 2D body are introduced and the former are expressed in terms of the latter by making some kinematical assumptions. The expressions for the strain and kinetic energy densities of the network are then introduced and given in terms of the kinematic quantities of the 2D continuum. In order to account for the modelling abilities of the 2D continuum in the linear range, the eigenmode and eigenfrequencies of a given specimen are determined. The buckling and postbuckling behaviour of the same specimen, subjected to two different loading conditions are analysed as tests in the nonlinear range. The problems have been solved numerically by means of COMSOL Multiphysics FE software.

1 Introduction

The type of pantographic structure considered in this paper can be described as follows. Consider a hyperelastic beam of uniform cross-section orthogonal to a straight axis. Take a set of these beams so that the cross sections have the same orientation and the axes are parallel and lie on a plane at a constant pitch. Then duplicate the set and rotate the new plane by $\pi/2$. Superpose the two planes and connect the beams where they cross each other by small cylinders that we will call 'pivots'. Finally cut a rectangle whose sides intersect the beam axes at $\pi/4$ (see fig.1).

Such structures, that we will refer to as 'pantographic', have been largely analysed in a number of preceding papers [1–12] where only specimens subject to planar motions have been studied.

The aim of this paper is to take into account also large, out of plane, motions.

This point can be addressed in a number of ways. One resides in assuming that each element of the structure is a 3D nonlinear hyperelastic Cauchy body [13]. Besides, one can assume that the beams are modelled as 1D continua (Euler, Timoshenko, or more sophisticated beams [14]). In both the cases, the solution even of simple problems requires a numerical approach that can lead to very cumbersome calculations, giving results that, due to their intrinsic complexity, may prove to be scarcely reliable. This is why to look for alternative approaches is necessary. The authors maintain that a way to overcome such difficulties can be found by modelling the pantographic structure as a 2D continuum endowed with a suitable internal structure.

As will be seen in the following, although the proposed model can not be able to describe the mechanical behaviour of the pantograph in a detailed way, it gives a fair account of many relevant phenomena both qualitatively and quantitatively.

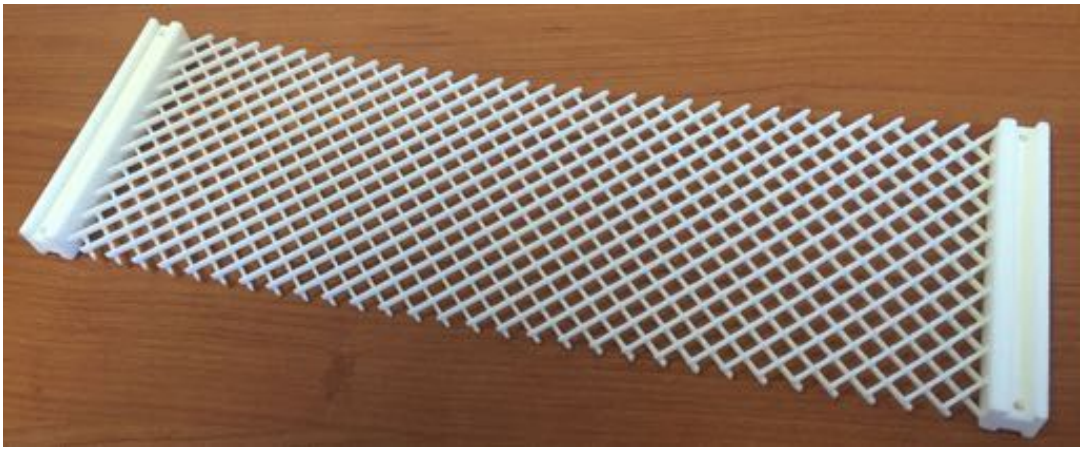

Figure 1: Sample of a pantographic sheet made up of polyamide by a 3D printing.

The procedure adopted takes into account some results presented in [15, 16] and can be arranged in the following steps.

At first the pantographic sheet is viewed as a beam network. This means that each beam is modelled as a nonlinear hyperelastic body whose motion is described by the placement of a line (the beam axis) and a rotation field that describes the placement of the beam cross-sections (assumed to behave as 2D rigid bodies). In addition, the assumption that the pivots can undergo only torsional deformation, is made. The distance between to adjacent pivots is assumed as the 'pitch' of the pantographic structure and is considered as a vanishing quantity.

The continuum chosen for describing the coarse behaviour of the pantographic sheet is a 2D (initially flat) body endowed with an internal structure characterised by two orthogonal tensor fields whose values at a point where two beams meet give account of their cross-section rotations.

The *equivalence* between the 2D model and the beam network is obtained by requiring that the strain energy density is the same for some selected classes of regular motions.

The assumption that the pivots can only undergo torsional deformation is shown to result in some internal constraints for the 2D model that allow to express both the rotation fields in terms of the transplacement of the 2D surface. The internal microstructure then becomes 'latent' (see [17]) with the consequence that the 2D continuum results to be of the second gradient type [18–28]. Using the reduced kinematics, an expression of the kinetic energy of the 2D body is derived from the one of the network by following an *equivalence* procedure analogous to that used for the strain energy described before. If compared with a classical plate model, the proposed 2D continuum is certainly more complex. This is due to the fact that it is aimed to describe, at least in an approximate way, the mechanical behaviour of the beams that make up the pantographic sheet. In order to do that the introduction of a microstructure richer than that used for standard plate, is compulsory. Of course, the larger is the number of the parameters introduced in the microstructure, the greater is the accuracy in the description of the behaviour of the beams. In this sense the proposed model can be certainly enriched in order to improve its simulation ability. Obviously, this is a cost that deserves to be carefully evaluated. It is worth adding that the proposed continuous model can be properly employed not only to describe the synthetic metamaterial we have in mind but also to describe biological phenomena characterised by

the presence of a lattice microstructure of fibres as in fibre-reinforced materials [29, 30], or trabecular bones [31, 32].

In order to test the model in the linear range the natural frequencies of a specimen have been evaluated. As a sample of nonlinear analysis, the buckling and postbuckling behaviour of the same specimen subjected to a uniform axial displacement along a part of the boundary has been analysed. Besides, the case of a tangential uniform displacement along the same side has been studied. We remark that the nonlinear analysis can be extended also to dynamic problems, and in particular to the wave propagation. In fact, nonlinearity associated with gradient elasticity can allow to capture, as it is well known, very interesting phenomena (see e.g. [33]). However, this kind of analysis is beyond the scope of this paper. All the numerical analyses have been made by means of the COMSOL Multiphysics® finite element software.

2 Planar beams' network

As a first step the pantographic structure described in the Introduction is modelled as a planar network of beams. This means that in the reference configuration, the straight axes of the two families of beams are assumed to lie in the same plane. They are denoted by ${}^{1j}\mathscr{C}$ with $j = \{1, .., b\}$, and ${}^{2i}\mathscr{C}$ with $i = \{1, .., a\}$, where the first left superscript (whose values are 1, 2) denotes the family and second the element of that family.

Now we make the following Assumptions on the constraints to the network:

Assumption 2.1) Where the beams' axes cross each other (joints), the points belonging to the two curves must share the same position in any configuration;

Assumption 2.2) Each beam is shear undeformable, that is, the cross sections remain orthogonal to the tangent vector at each point of the axis in any configuration;

Assumption 2.3) At the joints the cross sections of the two beams are rigidly connected apart from the rotation about the line in which they intersect, in view of Assumption 2.2, remains orthogonal to the tangent plane of the network.

On the reference network plane we define a Cartesian orthogonal coordinate system (X_1, X_2) whose associated base of unit vectors is $(\mathbf{D}_1, \mathbf{D}_2)$ which are chosen to be directed as ${}^{1j}\mathscr{C}$ and ${}^{2i}\mathscr{C}$, respectively. The unit vector normal to the network plane is $\mathbf{D}_3 = \mathbf{D}_1 \times \mathbf{D}_2$. We assume that the spacing between the beams of the network is the same for both the families and will be denoted by ℓ, so that:

- the coordinates of a point ${}^{1j}X \in {}^{1j}\mathscr{C}$ are $(X_1, j\ell)$;
- the coordinates of a point ${}^{2i}X \in {}^{2i}\mathscr{C}$ are $(i\ell, X_2)$.

In addition we put

- ${}^{\alpha}\mathbf{E}$ as the unit tangent vector directed along ${}^{\alpha h}\mathscr{C}$ where $\alpha = (1, 2)$ stands for the specific family and $h = (j, i)$ identifies the beam in the family;
- $\mathbf{N} = {}^{1}\mathbf{E} \times {}^{2}\mathbf{E}$;
- ${}^{\alpha}\mathbf{M} = \mathbf{N} \times {}^{\alpha}\mathbf{E}$.

where ${}^{\alpha}\mathbf{M}$ and $\mathbf{N}$ are assumed to be directed along the principal inertial axes of the beam cross sections. Besides we assume that ${}^{1}\mathbf{E}$, ${}^{1}\mathbf{M}$ coincide with $\mathbf{D}_1, \mathbf{D}_2$ respectively; ${}^{2}\mathbf{E}$, ${}^{2}\mathbf{M}$ coincide with $\mathbf{D}_2, -\mathbf{D}_1$, respectively, while $\mathbf{N} = \mathbf{D}_3$.

A deformed configuration of the beam axes ${}^{\alpha h}\mathscr{c}$ is described by the transplacements

$$\begin{aligned} {}^{\alpha h}\chi \quad : \quad & {}^{\alpha h}\mathscr{C} \to {}^{\alpha h}\mathscr{c} \\ & {}^{\alpha h}X \mapsto {}^{\alpha h}x \end{aligned} \tag{1}$$

and, in view of the Assumption 2.1, the following conditions must be satisfied: denoting by ${}^{ij}X$ the joint that in the reference configuration occupies the position with coordinates $(i\ell, j\ell)$

$${}^{1j}\chi({}^{ij}X) = {}^{2i}\chi({}^{ij}X) = {}^{ij}x \tag{2}$$

Now, we denote by

$${}^{\alpha h}\boldsymbol{t} = \frac{\partial\, {}^{\alpha h}\chi}{\partial X_\alpha} \tag{3}$$

the tangent vector to the curve ${}^{\alpha h}\mathscr{c}$ and by

$${}^{\alpha h}\boldsymbol{u} = {}^{\alpha h}\chi({}^{\alpha h}X) - {}^{\alpha h}X \tag{4}$$

the displacement of the beam axes.

The rotation of the cross sections is given by the orthogonal tensor fields

$${}^{\alpha h}\boldsymbol{R} : ({}^{\alpha}\mathbf{E},\ {}^{\alpha}\mathbf{M}, \mathbf{N}) \mapsto ({}^{\alpha h}\boldsymbol{e},\ {}^{\alpha h}\boldsymbol{m},\ {}^{\alpha h}\boldsymbol{n}) \tag{5}$$

where

$${}^{\alpha h}\boldsymbol{e} = \frac{{}^{\alpha h}\boldsymbol{t}}{\|{}^{\alpha h}\boldsymbol{t}\|} \tag{6}$$

is the unit tangent vector along the deformed axis ${}^{\alpha h}\mathscr{c}$, and Span$\{{}^{\alpha h}\boldsymbol{n}, {}^{\alpha h}\boldsymbol{m}\}$ define the new orientation of the cross sections [34–38].

In addition, in view of the Assumption 2.2, the following conditions must be satisfied

$${}^{1j}\boldsymbol{n}({}^{ij}X) = {}^{2i}\boldsymbol{n}({}^{ij}X) =: {}^{ij}\boldsymbol{n} \tag{7}$$

$${}^{ij}\boldsymbol{n} = \frac{{}^{1j}\boldsymbol{e} \times {}^{2i}\boldsymbol{e}}{\|{}^{1j}\boldsymbol{e} \times {}^{2i}\boldsymbol{e}\|} \tag{8}$$

$${}^{\alpha h}\boldsymbol{m} = {}^{ij}\boldsymbol{n} \times {}^{\alpha h}\boldsymbol{e} \tag{9}$$

The local deformation measures for the beam ${}^{\alpha h}()$ are assumed to be

$${}^{\alpha h}\varepsilon = \|{}^{\alpha h}\boldsymbol{t}\| - 1 \tag{10}$$

and the components of the skew tensor ${}^{\alpha h}\boldsymbol{W}(X_\alpha) = {}^{\alpha h}\boldsymbol{R}^T(X_\alpha)\, {}^{\alpha h}\boldsymbol{R}'(X_\alpha)$[1] which can be made explicit as follows

$${}^{\alpha h}\boldsymbol{W} = {}^{\alpha h}\kappa_1\, {}^{\alpha}\mathbf{M} \wedge \mathbf{N} + {}^{\alpha h}\kappa_2\ \mathbf{N} \wedge {}^{\alpha}\mathbf{E} + {}^{\alpha h}\kappa_3\, {}^{\alpha}\mathbf{E} \wedge {}^{\alpha}\mathbf{M}$$

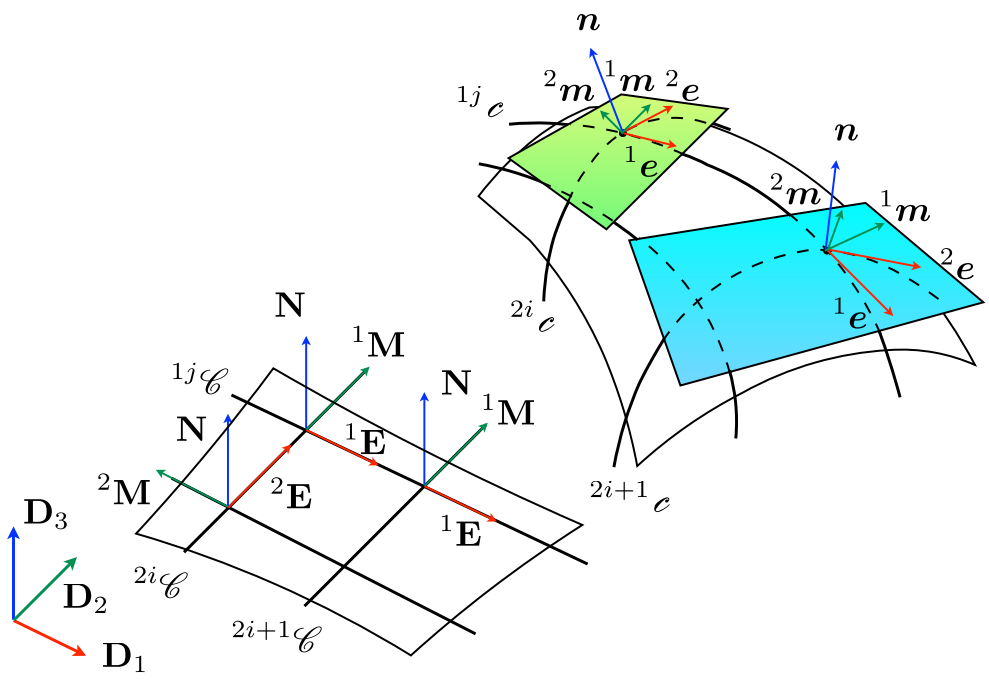

Figure 2: Scheme of the 2D continuum with local microstructure in the reference configuration and in the present one.

3 A 2D continuum with (latent) internal microstructure

Let us consider now a 2D continuum embedded in a 3D space as a surface at each point of which two 3D rigid bodies are attached.

We assume that in the reference configuration the surface is a rectangle $\mathcal{R}$ and the orientation of each one of the two rigid bodies are the same at each point of the 2D continuum (Fig. 2).

In the plane of the rectangle, a Cartesian coordinate system is introduced with the associated orthonormal base $(\mathbf{D}_1, \mathbf{D}_2, \mathbf{D}_3 = \mathbf{D}_1 \times \mathbf{D}_2)$. In this way a point $X \in \mathcal{R}$ will have the coordinates (X_1, X_2).

A deformed configuration can be identified by a transplacement

$$\begin{aligned} \chi \quad &: \quad \mathcal{R} \to \mathcal{S} \\ &\quad\;\; X \mapsto x \end{aligned} \tag{11}$$

and two orthogonal tensor fields

$$\begin{aligned} {}^1\boldsymbol{R} \quad &: \quad (\mathbf{D}_1, \mathbf{D}_2, \mathbf{D}_3) \mapsto ({}^1\mathbf{a}_1, {}^1\mathbf{a}_2, {}^1\mathbf{a}_3) \\ {}^2\boldsymbol{R} \quad &: \quad (\mathbf{D}_1, \mathbf{D}_2, \mathbf{D}_3) \mapsto ({}^2\mathbf{a}_1, {}^2\mathbf{a}_2, {}^2\mathbf{a}_3) \end{aligned} \tag{12}$$

[1]The prime symbol denotes differentiation of a function with respect to its own argument.

where $({}^1\mathbf{a}_1, {}^1\mathbf{a}_2, {}^1\mathbf{a}_3)$ and $({}^2\mathbf{a}_1, {}^2\mathbf{a}_2, {}^2\mathbf{a}_3)$ give the orientation of the microstructure in the deformed configuration as an effect of the rotations ${}^1\boldsymbol{R}$ and ${}^2\boldsymbol{R}$. We remark that the proposed continuum differs from a typical micropolar (or Cosserat-type) continuum as, e.g., proposed in [39, 40], because of the presence of two distinct rotations.

Finally, we will call

$$\boldsymbol{u}(X) = x - X = u_1(X)\mathbf{D}_1 + u_2(X)\mathbf{D}_2 + u_3(X)\mathbf{D}_3 \tag{13}$$

the displacement field defined on $\mathcal{R}$.

Now, we denote by

$${}^\alpha\boldsymbol{t} = \frac{\partial\, \chi}{\partial X_\alpha} \qquad \alpha = 1, 2 \tag{14}$$

the vectors tangent to the deformed coordinate lines, while

$${}^\alpha\boldsymbol{e} = \frac{{}^\alpha\boldsymbol{t}}{\|{}^\alpha\boldsymbol{t}\|} \tag{15}$$

are the corresponding *unitary* tangent vectors. In addition, we denote by

$$\boldsymbol{n} = \frac{{}^1\boldsymbol{e} \times {}^2\boldsymbol{e}}{\|{}^1\boldsymbol{e} \times {}^2\boldsymbol{e}\|} \tag{16}$$

the unit normal to the deformed surface.

The local deformation measures of the 2D continuum are assumed to be

$${}^\alpha\varepsilon = \|{}^\alpha\boldsymbol{t}\| - 1, \qquad {}^1\boldsymbol{e} \cdot {}^2\boldsymbol{e} = \sin\gamma \tag{17}$$

and

$$\begin{aligned} {}^1\boldsymbol{W} &:= {}^1\boldsymbol{R}^T \frac{\partial\, {}^1\boldsymbol{R}}{\partial X_1} = {}^1\kappa_1\ \mathbf{D}_2 \wedge \mathbf{D}_3 + {}^1\kappa_2\ \mathbf{D}_3 \wedge \mathbf{D}_1 + {}^1\kappa_3\ \mathbf{D}_1 \wedge \mathbf{D}_2 \\ {}^2\boldsymbol{W} &:= {}^2\boldsymbol{R}^T \frac{\partial\, {}^2\boldsymbol{R}}{\partial X_2} = {}^2\kappa_1\ \mathbf{D}_2 \wedge \mathbf{D}_3 + {}^2\kappa_2\ \mathbf{D}_3 \wedge \mathbf{D}_1 + {}^2\kappa_3\ \mathbf{D}_1 \wedge \mathbf{D}_2 \end{aligned} \tag{18}$$

Note that ${}^\alpha\varepsilon$ and γ represent the 'stretch' of the surface while the six components of ${}^1\boldsymbol{W}$ and ${}^2\boldsymbol{W}$ are 'curvatures' evaluated along the coordinate lines.

Now, we assume that the following constraints hold at each point $X \in \mathcal{R}$:

Constraint 1) ${}^1\boldsymbol{a}_1 = {}^1\boldsymbol{e}$ and ${}^2\boldsymbol{a}_1 = {}^2\boldsymbol{e}$

Constraint 2) ${}^1\boldsymbol{a}_3 = {}^2\boldsymbol{a}_3 = \boldsymbol{n}$

Constraint 3) ${}^1\boldsymbol{a}_2 = \boldsymbol{n} \times {}^1\boldsymbol{e}$ and ${}^2\boldsymbol{a}_2 = \boldsymbol{n} \times {}^2\boldsymbol{e}$

Due to these constraints, the rotations ${}^1\boldsymbol{R}, {}^2\boldsymbol{R}$, and consequently the orientation of the two rigid bodies that describe the local microstructure at X, *are completely determined by the present shape of the coordinate lines passing through the point* X. This means that the local structure becomes *latent* in the sense of [17].

It is also worth noting that, due to the constraints introduced, γ results to be the amplitude of the relative rotation between the two rigid bodies that describe the microstructure at X.

The strain measures, written in terms of the displacement components, result to be

$$
{}^1\kappa_1 = -\frac{\boldsymbol{n}\cdot\boldsymbol{g}_1 - \sin\gamma\ \boldsymbol{n}\cdot\boldsymbol{c}_1}{\|{}^1\boldsymbol{e}\times{}^2\boldsymbol{e}\|} \quad {}^1\kappa_2 = \boldsymbol{n}\cdot\boldsymbol{c}_1 \quad {}^1\kappa_3 = -{}^1\boldsymbol{m}\cdot\boldsymbol{c}_1
$$

$$
{}^2\kappa_1 = \frac{\boldsymbol{n}\cdot\boldsymbol{g}_2 - \sin\gamma\ \boldsymbol{n}\cdot\boldsymbol{c}_2}{\|{}^1\boldsymbol{e}\times{}^2\boldsymbol{e}\|} \quad {}^2\kappa_2 = \boldsymbol{n}\cdot\boldsymbol{c}_2 \quad {}^2\kappa_3 = -{}^2\boldsymbol{m}\cdot\boldsymbol{c}_2 \tag{19}
$$

where ${}^\alpha\boldsymbol{m} = \boldsymbol{n}\times{}^\alpha\boldsymbol{e}$. The expressions for $\boldsymbol{c}_1, \boldsymbol{c}_2, \boldsymbol{g}_1, \boldsymbol{g}_2$ are given in the Appendix.

Note that

$$
{}^\alpha\kappa_1 = \frac{\partial\boldsymbol{n}}{\partial X_\alpha}\cdot{}^\alpha\boldsymbol{m}, \quad {}^\alpha\kappa_2 = \frac{\partial\,{}^\alpha\boldsymbol{e}}{\partial X_\alpha}\cdot\boldsymbol{n}, \quad {}^\alpha\kappa_3 = \frac{\partial\,{}^\alpha\boldsymbol{m}}{\partial X_\alpha}\cdot{}^\alpha\boldsymbol{e}, \tag{20}
$$

as the frames that describe the cross-sections can be interpreted as Darboux frames. In view of the assumed constraints, ${}^\alpha\kappa_1$, ${}^\alpha\kappa_2$, ${}^\alpha\kappa_3$ are the geodesic torsion, the normal curvature and the geodesic curvature multiplied by $\|{}^\alpha\boldsymbol{t}\|$, respectively, as X_α is not a unitary speed parametrisation.

Expression (19) can be obtained from expressions (18) following the procedures sketched in the Appendix.

4 The Planar beams' network as a 2D continuum

In this section, the 2D model introduced in Section 3 is used in order to give a coarse description of the mechanical behaviour of the network described in Section 2.

We make the following Assumptions:

Assumption 4.1) The network's joint ${}^{ij}X$ whose coordinates in the reference position are $(i\ell, j\ell)$ is identified with the point X of the continuum that share the same reference coordinates [41].

Assumption 4.2) The axes of the two network beams that lie along the coordinate lines through ${}^{ij}X$ are identified with the corresponding coordinate lines through the point X in the 2D continuum; the sections attached to the beam axes along X_1, X_2 are identified with the rigid bodies of the 2D continuum denoted by the subscripts $1, 2$, respectively.

Using the definitions introduced in the Sections 2 and 3 the local deformation measures of the 2D continuum are assumed to be

$$
{}^\alpha\varepsilon = {}^{\alpha h}\varepsilon, \qquad {}^1\boldsymbol{e}\cdot{}^2\boldsymbol{e} = {}^{1j}\boldsymbol{e}\cdot{}^{2i}\boldsymbol{e} = \sin\gamma \tag{21}
$$

where ${}^\alpha\boldsymbol{t}$ are the vectors defined in (14), and

$$
{}^1\boldsymbol{W} = {}^{1h}\boldsymbol{W}(X_1), \qquad {}^2\boldsymbol{W} = {}^{2h}\boldsymbol{W}(X_2) \tag{22}
$$

that is, in components

$$
{}^\alpha\kappa_1 = {}^{\alpha h}\kappa_1, \quad {}^\alpha\kappa_2 = {}^{\alpha h}\kappa_2, \quad {}^\alpha\kappa_3 = {}^{\alpha h}\kappa_3 \tag{23}
$$

Note that, in view of $(21)_2$, the relative rotation of the two rigid bodies attached at a point of the 2D body, is identified with the relative rotation of the tangents to the two beams of the network crossing at that point which, in turn, describes the torsion of a pivot.

Due to the constraints introduced both the shear deformation in the beams and pivots has been disregarded. This assumption seems to be fair, generally speaking. However, when one requires a metamaterial in which the sliding between the two families of beams should be allowed, at least the shear deformation of the pivots must be taken into account.

5 Energy and dynamical equations

Let us consider now a Representative Elementary Volume (REV) which is a square of edge length ℓ centred at a network's joint ${}^{ij}X$.

The strain energy density of the 2D continuum is assumed to be

$$\pi = \frac{1}{2}\left[\mathrm{K}_e({}^1\varepsilon^2 + {}^2\varepsilon^2) + \mathrm{K}_s\gamma^2 + \mathrm{K}_t\ ({}^1\kappa_1^2 + {}^2\kappa_1^2) + \mathrm{K}_n\ ({}^1\kappa_2^2 + {}^2\kappa_2^2) + \mathrm{K}_g\ ({}^1\kappa_3^2 + {}^2\kappa_3^2)\right] \tag{24}$$

where

$$\mathrm{K}_e = \frac{YA}{\ell}, \quad \mathrm{K}_s = \frac{GJ_p}{h_p\,\ell^2}, \quad \mathrm{K}_t = \frac{GJ_t}{\ell}, \quad \mathrm{K}_n = \frac{YJ_{f1}}{\ell}, \quad \mathrm{K}_g = \frac{YJ_{f2}}{\ell} \tag{25}$$

G being the shear modulus, J_p the torsional inertia of the pivot and $J_t,\ J_{f1},\ J_{f2}$ the torsional and flexural inertia of the beams' cross-sections (see e.g. [42,43] and [44] for an identification method suitable for the polyamide).

Note that K_e, K_t, K_n and K_g are the stiffnesses related to the elongation, twisting, normal and geodesic bending, of the beams embedded in the REV; while K_s is the shear stiffness between beams belonging to the two different families.

The angular velocity of the beam cross-sections, is described by the skew tensor field

$${}^{\alpha}\boldsymbol{V} := {}^{\alpha}\boldsymbol{R}^T\,{}^{\alpha}\dot{\boldsymbol{R}} = {}^{\alpha}\omega_1\mathbf{D}_2\wedge\mathbf{D}_3 + {}^{\alpha}\omega_2\mathbf{D}_3\wedge\mathbf{D}_1 + {}^{\alpha}\omega_3\ \mathbf{D}_1\wedge\mathbf{D}_2$$

where the dot denotes the time derivative.

The kinetic energy density is

$$\tau = \frac{1}{2}\varrho_s(\dot{u}_1^2 + \dot{u}_2^2 + \dot{u}_3^2) + \frac{1}{2}\left[J_1({}^1\omega_1{}^2 + {}^2\omega_1{}^2) + J_2({}^1\omega_2{}^2 + {}^2\omega_2{}^2) + J_3({}^1\omega_3{}^2 + {}^2\omega_3{}^2)\right] \tag{26}$$

where

$$\mathrm{J}_1 = \frac{\varrho\,J_t}{\ell}, \quad \mathrm{J}_2 = \frac{\varrho\,J_{f1}}{\ell}, \quad \mathrm{J}_3 = \frac{\varrho\,J_{f2}}{\ell} \tag{27}$$

ϱ_s being the apparent mass density per unit area and ϱ the apparent mass density.

Note that J_2 and J_3 are the moments of inertia of the beam cross-section with respect to the principal inertia axes, that is ${}^{\alpha}\mathbf{M}$, $\mathbf{N}$ (see Section 2) while J_1, is the polar moment of inertia evaluated with respect to the centre of the section.

The virtual work equation runs as follows

$$\delta\mathscr{W}_{(\mathrm{e})} + \delta\mathscr{W}_{(\mathrm{i})} + \delta\mathscr{W}_{(\mathrm{s})} + \delta\mathscr{W}_{(\mathrm{l})} = 0 \tag{28}$$

where the internal elastic work done on a given subdomain $\mathscr{B}$ of $\mathcal{R}$ is

$$\delta\mathscr{W}_{(\mathrm{e})} = -\int_{\mathscr{B}} \delta\pi\,\mathrm{d}S \tag{29}$$

and the inertial work can be expressed by

$$\delta\mathscr{W}_{(\mathrm{i})} = \int_{\mathscr{B}} \delta\tau \, \mathrm{d}S \tag{30}$$

or, after an integration by part, in an explicit form as reported in Appendix.

The external forces acting on $\mathscr{B}$ are the surface forces, exerted by systems located outside $\mathcal{R}$ which give the virtual work

$$\delta\mathscr{W}_{(\mathrm{s})} = \int_{\mathscr{B}} F_i \delta u_i \, \mathrm{d}S \tag{31}$$

and the contact forces acting on $\mathscr{B}$ by the parts of $\mathcal{R}$ located outside $\mathscr{B}$ which yield the virtual work

$$\delta\mathscr{W}_{(\mathrm{l})} = \int_{\partial\mathscr{B}} f_i \delta u_i \, \mathrm{d}l \tag{32}$$

We remark that because of the nature of the Eq. (24), which involves the second gradient of the independent displacement field $\boldsymbol{u}$, the proposed 2D continuum is also able to sustain double forces and corner forces. In what follows, for the sake of simplicity, we impose only geometric boundary conditions.

6 Numerical examples

Let us consider a rectangular specimen made up by two families of beams that in the reference configuration are orthogonal (see Fig. 1) and directed along $\mathbf{D}_1$ and $\mathbf{D}_2$, respectively. The edges of the specimen are directed along $\mathbf{B}_1$ and $\mathbf{B}_2$ obtained by a counterclockwise rotation of $\pi/4$ of $\mathbf{D}_1$ and $\mathbf{D}_2$. Their lengths are 21 cm and 7 cm along $\mathbf{B}_1$ and $\mathbf{B}_2$, respectively.

The beams have both rectangular cross-sections of area A and dimensions 1×1.6 mm while the pivot are cylinders long 1 mm and with circular cross-sections of diameter 0.9 mm. The pitch between two adjacent beams is $\ell = 7/\sqrt{2}$ mm. The beams and the pivots are made by polyamide. The material is assumed to be linear hyperelastic and isotropic with Young's modulus $Y = 1600$ MPa and Poisson's coefficient $\nu = 0.3$.

The specimen is modelled by the 2D body described in Section 4 that in the reference configuration is a rectangle with the same dimensions of the specimen, that is 7 and 21 cm.

As a first example, we consider the case in which the specimen is restrained along the shortest sides. One of them is fixed ($\boldsymbol{u} = \mathbf{0}$, ${}^1\boldsymbol{R} = \mathbf{I}$ and ${}^2\boldsymbol{R} = \mathbf{I}$ where $\mathbf{I}$ is the identity tensor) while the other can slide in the plane of the figure in the direction orthogonal to it ($\boldsymbol{u} = -\lambda\mathbf{B}_1$ with $\lambda \geqslant 0$, ${}^1\boldsymbol{R} = \mathbf{I}$ and ${}^2\boldsymbol{R} = \mathbf{I}$).

When λ reaches the value of 5.6 cm, an out of plane buckling is detected (see Figs. 3 and 4_a). The corresponding critical load is find to be about 5.8 N. The map of the strain energy density in that configuration is given in Fig. 4_b while the contributions of the deformation terms are shown in Fig. 5.

Furthermore, the case in which the boundary conditions on the moving side are changed in $\boldsymbol{u} = -\lambda\mathbf{B}_2$ with $\lambda \geqslant 0$, ${}^1\boldsymbol{R} = \mathbf{I}$ and ${}^2\boldsymbol{R} = \mathbf{I}$, which corresponds to a tangential uniform displacement, is examined. The first two critical values of λ are found to be about 2.2 cm and 4.7 cm (see Fig. 6_a) and the corresponding critical loads are about 10 N and 23.5 N, respectively (see Fig. 6_b). Note that the coordinates of point P_b referred to in Fig. 6 are $((23/30L)/\sqrt{(2)}, (l + 23/30L)/\sqrt{(2)})$. P_b is a point that shows an out-of-plane displacement very close to the maximum value. The first two bifurcation modes are reported in the Figs. 7_a and 7_b, respectively. The map of the contributions to the strain energy density in the first configuration, with out-of-plane antisymmetric peaks, is given in Fig. 8.

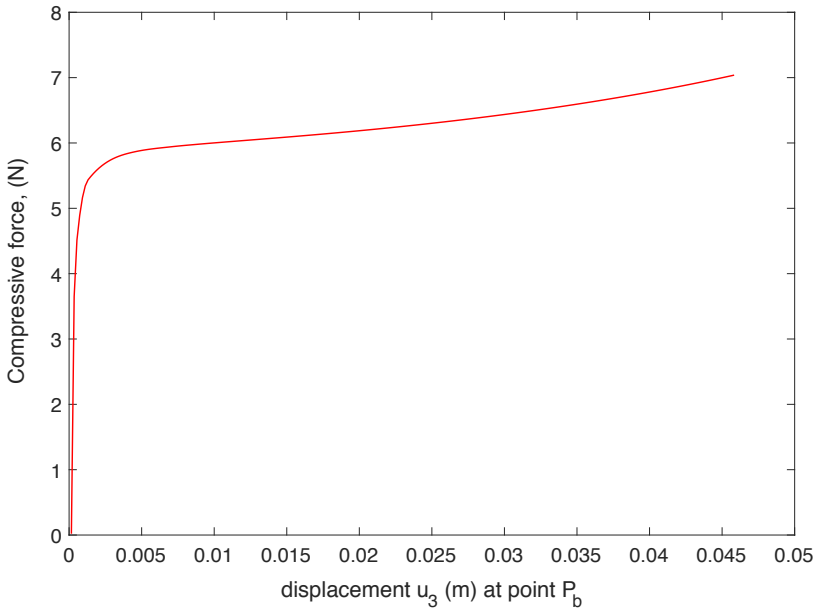

Figure 3: Compressive force vs out of plane displacement at the central point of the sample.

In order to test the dynamical behaviour of the specimen, the vibrations around two different configurations have been examined. They are obtained by putting $\lambda = 0$ and $\lambda = 49$ mm in the first example. We will refer to them as reference and pre-stretched respectively. Note that the value $\lambda = 49$ mm is 70% of the side length. The first twelve vibration modes have been determined for both the cases. In order to increase the mass of the beams, their sections have been given the following dimensions: 2.5×1.6 mm.

Figures 9–12 show the modal shapes associated to each one of the natural frequencies. The modal shapes are normalised to unit modal mass. The strain (Figs. 9 and 11) and kinetic (Figs. 10 and 12) energies are also reported by means of a superimposed colour map. Tables 1 and 2 summarise the eigenfrequencies for both the cases analysed, emphasising the effect of the section inertia, which at low frequencies can be neglected even if there are some small effects when the twisting energy involved is significant.

The cases examined have been solved numerically by using the 'Weak Form PDE' feature of COMSOL Multiphysics. This means that Eq. (28) has been explicitly coded while the FE discretisation has been made using the Argyris elements characterised by 21 degrees of freedom already implemented in COMSOL Multiphysics. The choice of Argyris elements has been done in order to guarantee C^1 continuity. Indeed, such elements can be used to properly approximate functions in the Sobolev space H^2, as those involved in our problem characterised by the presence of second spatial derivatives of the transplacement. To solve the problem in a more efficient way, ad hoc codes can be implemented by using an isogeometric formulation [45–47] or discrete Hencky-type systems based on the geometry of the microstructure as done in [48–50]. It is worth mentioning also particular adaptation of standard FEM for second gradient materials (see e.g. [51, 52]).

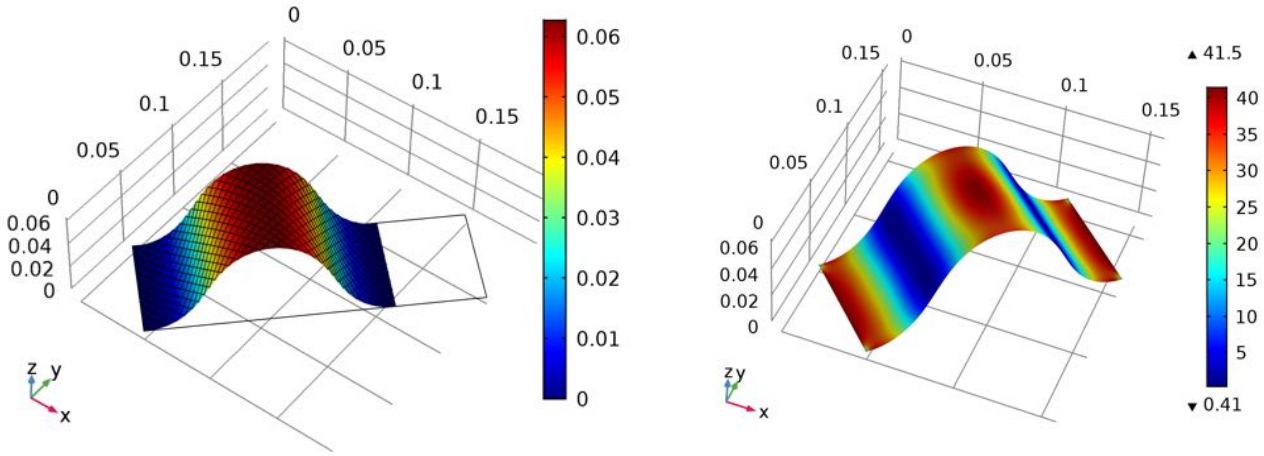

(a) Buckled shape

(b) Energy density map

Figure 4: Specimen subjected to edge displacement along $\mathbf{B}_1$.

Table 1: Reference configuration: eigenfrequencies, rad/s.

Mode #	with cross-section inertia	without cross-section inertia	difference %
1	593.93	594.10	0.02
2	1393.3	1393.4	0.01
3	1522.2	1525.1	0.19
4	1615.0	1615.1	0.01
5	1636.6	1637.8	0.07
6	3192.0	3199.6	0.24
7	3207.4	3212.6	0.16
8	3596.6	3597.4	0.02
9	3630.9	3631.7	0.02
10	5142.0	5158.3	0.32
11	5298.2	5313.0	0.28
12	6046.7	6091.0	0.73

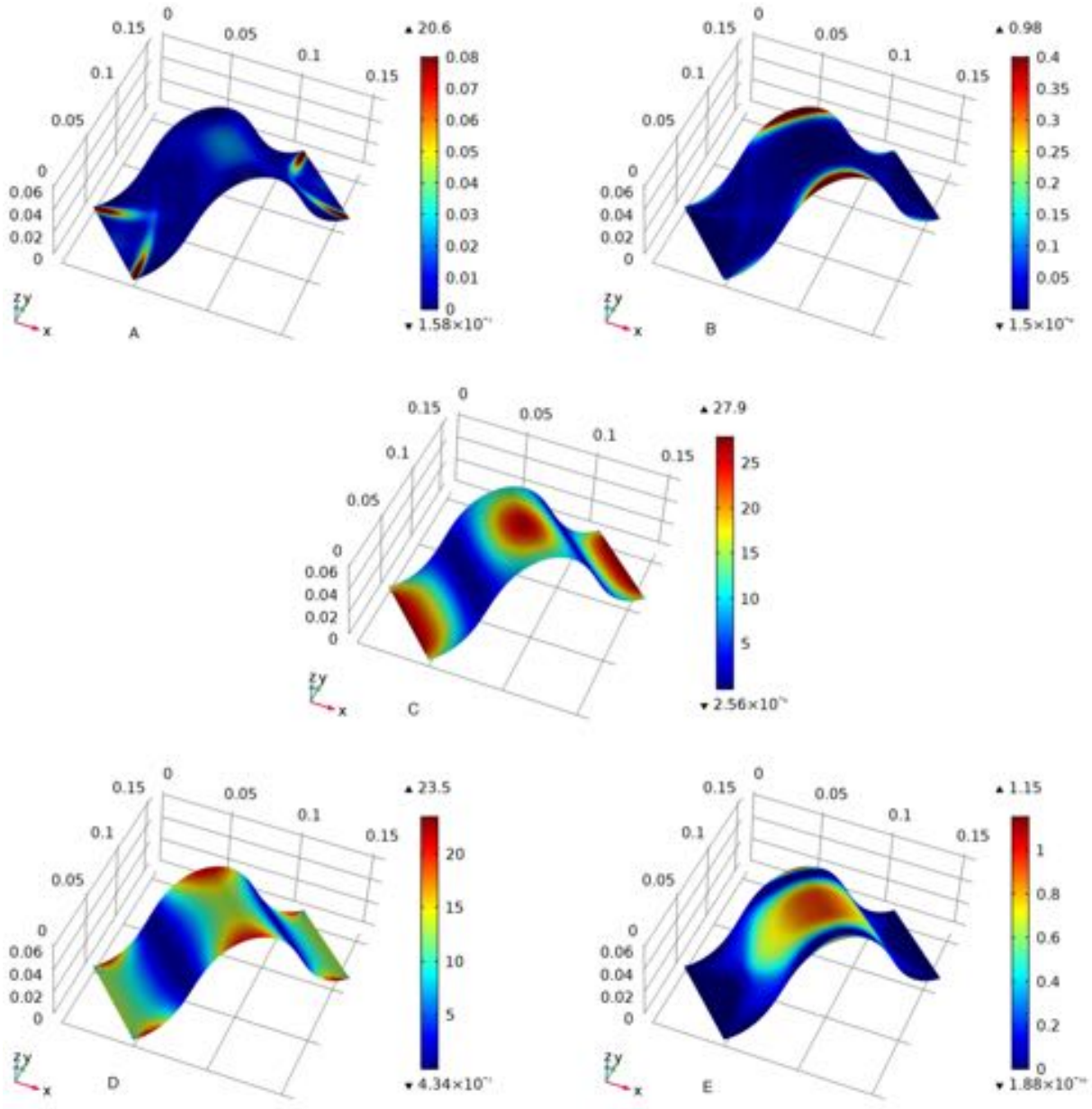

Figure 5: Energy density contributions. Extension a), geodesic bending b), normal bending c), twisting d) and shear e) energy densities.

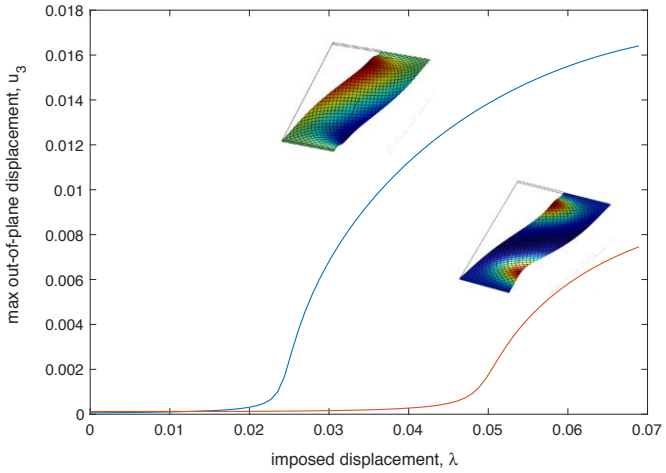

(a) Out-of-plane displacement of point P_b vs imposed displacement

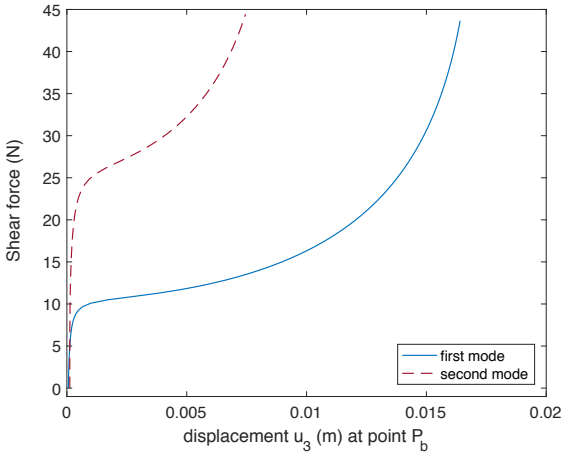

(b) Shear force vs out-of-plane displacement of point P_b

Figure 6: Specimen subjected to edge displacement along $\mathbf{B}_2$.

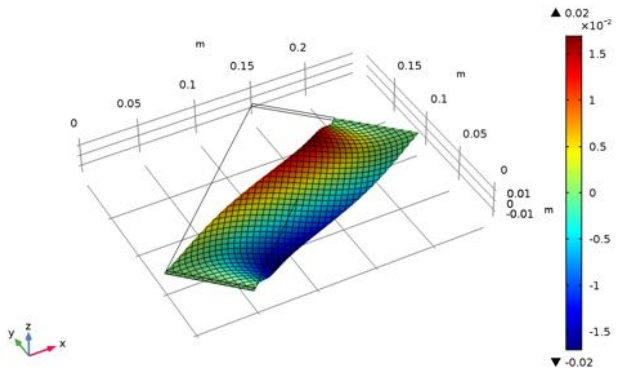

(a) First buckling mode

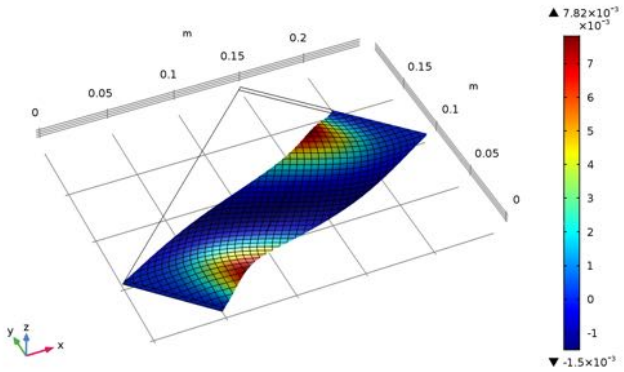

(b) Second buckling mode

Figure 7: Shear test: Buckled shapes of the first two bifurcation modes. Colours indicate values of the out-of-plane displacement.

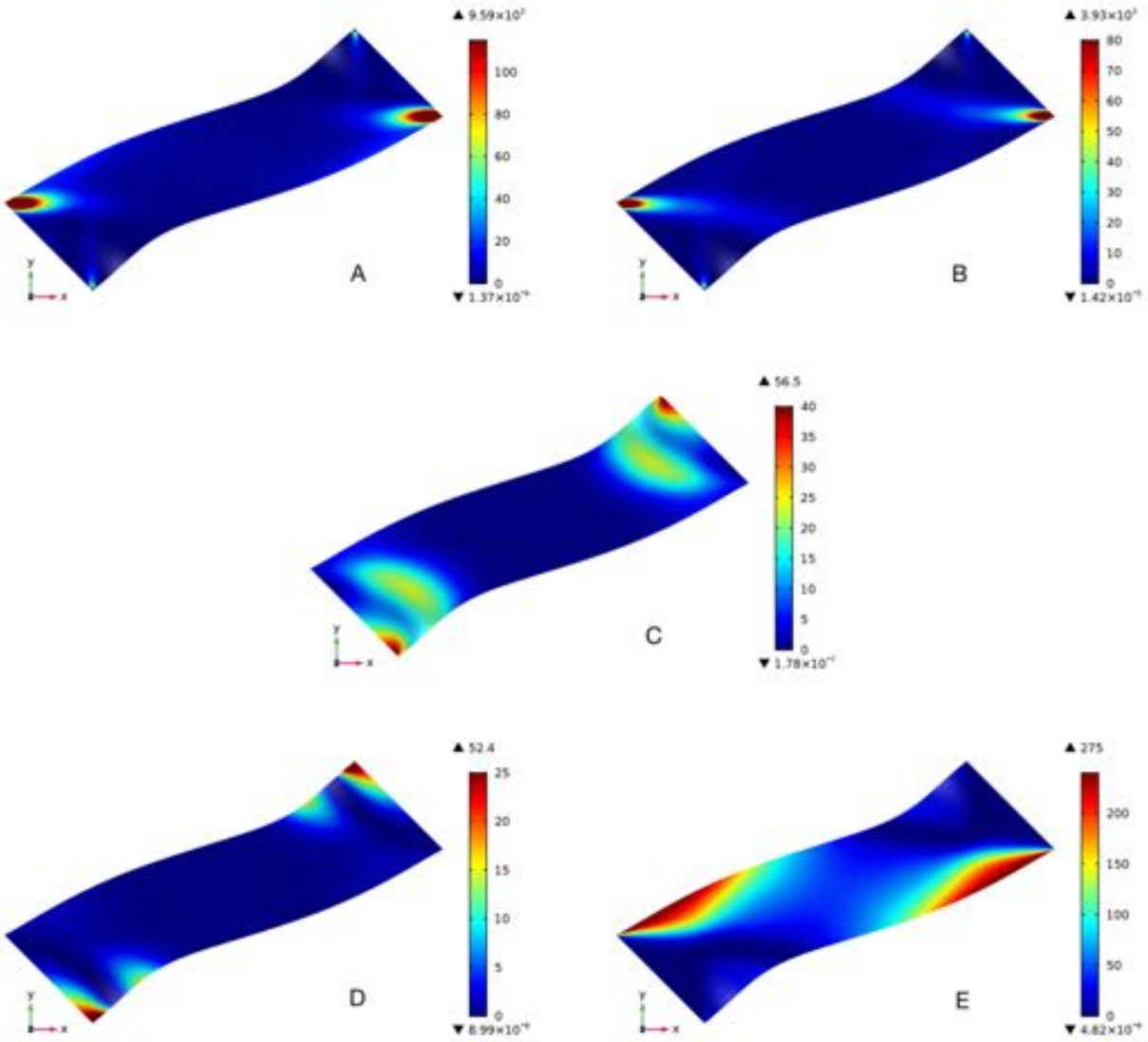

Figure 8: Shear test: Energy density contributions. Extension a), geodesic bending b), normal bending c), twisting d) and shear e) energy densities.

Table 2: Pre-stretched configuration: eigenfrequencies, rad/s.

Mode #	with cross-section inertia	without cross-section inertia	difference %
1	720.22	720.30	0.01
2	1597.3	1611.4	0.88
3	1671.0	1671.0	0.00
4	1774.5	1775.2	0.04
5	3044.3	3044.6	0.01
6	3163.5	3166.2	0.09
7	3899.7	3924.7	0.64
8	4189.7	4190.4	0.02
9	4744.6	4745.7	0.02
10	4944.8	4952.0	0.15
11	5889.7	6029.4	2.37
12	6818.8	6821.1	0.03

7 Conclusion

Pantographic structures made up by two families of equispaced beams, superimposed and connected by pivots, have been modelled at first as a plane network of beams, and then as a 2D continuum with a suitable internal structure. The internal structure has been made latent by imposing some internal constraints. A procedure aimed to express the kinematic variables of the beam network in terms of the ones of the 2D body that we have considered as coarse descriptors, has been described. Given an expression of the strain and kinetic energy densities for the beams, the corresponding energies of the network has been derived. By introducing the coarse descriptors in the preceding expressions, the energies of the 2D body have been constructed. The model obtained has been used for the analysis of the mechanical behaviour of a given specimen. The COMSOL Multiphysics FE software has been used in order to determine the eigenmode and eigenfrequencies of the specimen. For two different loading conditions, the nonlinear behaviour of the specimen has been determined, and the uprising of bifurcation detected and examined. It is worth mentioning that some laboratory tests on the specimen studied in this paper have been planned and will be shortly performed. They are intended to be a benchmark for the results obtained numerically.

8 Appendix

The expressions for the variables $\boldsymbol{c}_1, \boldsymbol{c}_2, \boldsymbol{g}_1, \boldsymbol{g}_2$ appearing in the deformation measures (19) are

$$\boldsymbol{c}_1 = \frac{(\nabla\nabla\chi)\mathbf{D}_1 \otimes \mathbf{D}_1}{\|\nabla\chi\ \mathbf{D}_1\|} \qquad \boldsymbol{c}_2 = \frac{(\nabla\nabla\chi)\mathbf{D}_2 \otimes \mathbf{D}_2}{\|\nabla\chi\ \mathbf{D}_2\|}$$

$$\boldsymbol{g}_1 = \frac{(\nabla\nabla\chi)\mathbf{D}_2 \otimes \mathbf{D}_1}{\|\nabla\chi\ \mathbf{D}_2\|} \qquad \boldsymbol{g}_2 = \frac{(\nabla\nabla\chi)\mathbf{D}_1 \otimes \mathbf{D}_2}{\|\nabla\chi\ \mathbf{D}_1\|}$$

The curvatures (19) can be obtained from Eqs. (18) following the procedure sketched below

$$
\begin{aligned}
{}^{\alpha}\boldsymbol{R} \quad : \quad & (\mathbf{D}_1, \mathbf{D}_2, \mathbf{D}_3) \mapsto ({}^{\alpha}\mathbf{a}_1, {}^{\alpha}\mathbf{a}_2, {}^{\alpha}\mathbf{a}_3) \\
& ({}^{\alpha}\boldsymbol{R}\mathbf{D}_i)' = {}^{\alpha}\boldsymbol{R}'\mathbf{D}_i = {}^{\alpha}\mathbf{a}_i{}' \\
& {}^{\alpha}\mathbf{a}_i{}' \cdot {}^{\alpha}\mathbf{a}_j = {}^{\alpha}\boldsymbol{R}'\mathbf{D}_i \cdot {}^{\alpha}\boldsymbol{R}\mathbf{D}_j = ({}^{\alpha}\boldsymbol{W}\mathbf{D}_i) \cdot \mathbf{D}_j = \varepsilon_{sij}{}^{\alpha}\kappa_s
\end{aligned} \tag{33}
$$

The explicit expression for the inertial virtual work of Eq. (30) is

$$
\begin{aligned}
\delta\mathscr{W}_{(\mathrm{i})} \quad = \quad & \int_{\mathscr{B}} -\varrho_s \left(\ddot{u}_1\delta u_1 + \ddot{u}_2\delta u_2 + \ddot{u}_3\delta u_3\right) + \\
& \sum_{\alpha}\{-J_2\left[\left(\boldsymbol{n} \cdot^{\alpha} \ddot{\boldsymbol{e}}\right)\boldsymbol{n} + \left(\dot{\boldsymbol{n}} \cdot^{\alpha} \dot{\boldsymbol{e}}\right)\boldsymbol{n} + \left(\boldsymbol{n} \cdot^{\alpha} \dot{\boldsymbol{e}}\right)\dot{\boldsymbol{n}}\right] + J_3\left({}^{\alpha}\boldsymbol{e} \cdot^{\alpha} \dot{\boldsymbol{m}}\right)^{\alpha}\dot{\boldsymbol{m}}\} \cdot \delta^{\alpha}\boldsymbol{e} + \\
& \sum_{\alpha}\{-J_3\left[\left({}^{\alpha}\boldsymbol{e} \cdot^{\alpha} \ddot{\boldsymbol{m}}\right)^{\alpha}\boldsymbol{e} + \left({}^{\alpha}\dot{\boldsymbol{e}} \cdot^{\alpha} \dot{\boldsymbol{m}}\right)^{\alpha}\boldsymbol{e} + \left({}^{\alpha}\boldsymbol{e} \cdot^{\alpha} \dot{\boldsymbol{m}}\right)^{\alpha}\dot{\boldsymbol{e}}\right] + J_1\left({}^{\alpha}\boldsymbol{m} \cdot \dot{\boldsymbol{n}}\right)\dot{\boldsymbol{n}}\} \cdot \delta^{\alpha}\boldsymbol{m} + \\
& \sum_{\alpha}\{-J_1\left[\left({}^{\alpha}\boldsymbol{m} \cdot \ddot{\boldsymbol{n}}\right)^{\alpha}\boldsymbol{m} + \left({}^{\alpha}\dot{\boldsymbol{m}} \cdot \dot{\boldsymbol{n}}\right)^{\alpha}\boldsymbol{m} + \left({}^{\alpha}\boldsymbol{m} \cdot \dot{\boldsymbol{n}}\right)^{\alpha}\dot{\boldsymbol{m}}\right] + J_2\left(\boldsymbol{n} \cdot^{\alpha} \dot{\boldsymbol{e}}\right)^{\alpha}\dot{\boldsymbol{e}}\} \cdot \delta\boldsymbol{n}\,\mathrm{d}S
\end{aligned} \tag{34}
$$

References

[1] Wang W-B, Pipkin AC. 1987 Plane deformations of nets with bending stiffness. *Acta Mech.* **65**, 263–279. (doi:10.1007/BF01176886)

[2] Steigmann DJ, Pipkin AC. 1991 Equilibrium of elastic nets. *Phil. Trans. R. Soc. Lond.* **335**, 419–454. (http://www.jstor.org/stable/53796)

[3] dell'Isola F, Lekszycki T, Pawlikowski M, Grygoruk R, Greco L. 2015 Designing a light fabric metamaterial being highly macroscopically tough under directional extension: first experimental evidence. *Z. Angew. Math. Phys.*, vol. **66**, Issue 6, 3473–3498 (doi:10.1007/s00033-015-0556-4)

[4] dell'Isola F, Della Corte A, Greco L, Luongo A. 2016 Plane bias extension test for a continuum with two inextensible families of fibers: a variational treatment with Lagrange multipliers and a perturbation solution. *Int. J. Solids Struct.*, **81**, 1–12, (doi:10.1016/j.ijsolstr.2015.08.029)

[5] dell'Isola F, Cuomo M, Greco L, Della Corte A. 2017 Bias extension test for pantographic sheets: numerical simulations based on second gradient shear energies. *J. Eng. Math.*, **103**, 127–157. (doi:10.1007/s10665-016-9865-7)

[6] Cuomo M, dell'Isola F, Greco L. 2016 Simplified analysis of a generalized bias test for fabrics with two families of inextensible fibres, *Z. Angew. Math. Phys.*, **67**, 1–23. (doi:10.1007/s00033-016-0653-z)

[7] dell'Isola F, Steigmann D, Della Corte A. 2016 Synthesis of Fibrous Complex Structures: Designing Microstructure to Deliver Targeted Macroscale Response. *ASME. Appl. Mech. Rev.* **67**, 060804-060804–21. (doi:10.1115/1.4032206)

[8] dell'Isola F, Steigmann D. 2015 A two-dimensional gradient-elasticity theory for woven fabrics. *J. Elasticity* **118**, 113–125. (doi:10.1007/s10659-014-9478-1)

[9] dell'Isola F, Giorgio I, Pawlikowski M, Rizzi NL. 2016 Large deformations of planar extensible beams and pantographic lattices: heuristic homogenization, experimental and numerical examples of equilibrium. *Proc. R. Soc. A*, vol. **472** Issue 2185 (20150790); (doi:10.1098/rspa.2015.0790).

[10] Turco E, Golaszewski M, Giorgio I, D'Annibale F. 2017 Pantographic lattices with non-orthogonal fibres: Experiments and their numerical simulations. *Compos. Part B Eng.*, **118**, 1–14. (doi:10.1016/j.compositesb.2017.02.039)

[11] Spagnuolo M, Barcz K, Pfaff A, dell'Isola F, Franciosi P. 2017 Qualitative pivot damage analysis in aluminum printed pantographic sheets: Numerics and experiments, *Mech. Res. Commun.*, **83**, 47–52, (doi:10.1016/j.mechrescom.2017.05.005)

[12] Barchiesi E, Placidi L. (2017) A Review on Models for the 3D Statics and 2D Dynamics of Pantographic Fabrics. In: Sumbatyan M. (eds) *Wave Dynamics and Composite Mechanics for Microstructured Materials and Metamaterials*. Advanced Structured Materials, vol **59**, 239–258. Springer, Singapore. (doi:10.1007/978-981-10-3797-9_14)

[13] Giorgio I. 2016 Numerical identification procedure between a micro-Cauchy model and a macro-second gradient model for planar pantographic structures. *Z. Angew. Math. Phys.*, **67**, 95-1–17. (doi:10.1007/s00033-016-0692-5)

[14] Harrison P. 2016 Modelling the forming mechanics of engineering fabrics using a mutually constrained pantographic beam and membrane mesh, *Compos. A Appl. Sci. Manuf.*, **81**, 145–157. (doi:10.1016/j.compositesa.2015.11.005)

[15] Steigmann DJ, dell'Isola F. 2015 Mechanical response of fabric sheets to three-dimensional bending, twisting, and stretching. *Acta Mech. Sinica* **31**, 373–382. (doi:10.1007/s10409-015-0413-x)

[16] Steigmann DJ. 2017 Equilibrium of elastic lattice shells. *J. Eng. Math.* (doi:10.1007/s10665-017-9905-y)

[17] Capriz G. 1987 Continua with latent microstructure. In: *Analysis and Thermodynamics* (A collection o papers dedicated to W. Noll on his sixties birthday), Eds. B. Coleman, M. Freinberg and J. Serrin pp- 161–174, Springer-Verlag, New York. (doi:10.1007/978-3-642-61598-6_9)

[18] dell'Isola F, Andreaus U, Placidi L. 2015 At the origins and in the vanguard of peridynamics, non-local and higher gradient continuum mechanics. An underestimated and still topical contribution of Gabrio Piola, *Math. Mech. Solids*, **20**, 887–928. (doi:10.1177/1081286513509811)

[19] Eugster SR, dell'Isola F. 2017 Exegesis of the Introduction and Sect. I from "Fundamentals of the Mechanics of Continua" by E. Hellinger, *Z. Angew. Math. Mech.*, **97**, 477–506. (doi:10.1002/zamm.201600108)

[20] Eugster SR, dell'Isola F. 2017 Exegesis of Sect. II and III.A from "Fundamentals of the Mechanics of Continua" by E. Hellinger, *Z. Angew. Math. Mech.*, 1–38. (doi:10.1002/zamm.201600293)

[21] Germain P. 1973 The Method of Virtual Power in Continuum Mechanics. Part 2: Microstructure, *SIAM J. Appl. Math.*, **25**, 556–575. (doi:10.1137/0125053)

[22] Alibert J-J, Seppecher P, dell'Isola F. 2003 Truss modular beams with deformation energy depending on higher displacement gradients. *Math. Mech. Solids* **8**, 51–73. (doi:10.1177/1081286503008001658)

[23] Seppecher P, Alibert J-J, dell'Isola F. 2011 Linear elastic trusses leading to continua with exotic mechanical interactions. *J. Phys. Conf. Ser.* **319**, 012018. (doi:10.1088/1742-6596/319/1/012018)

[24] Alibert J-J, Della Corte A. 2015 Second-gradient continua as homogenized limit of pantographic microstructured plates: a rigorous proof. *Z. Angew. Math. Phys.* **66**, 2855–2870. (doi:10.1007/s00033-015-0526-x)

[25] Carcaterra A, dell'Isola F, Esposito R, Pulvirenti M. 2015 Macroscopic description of microscopically strongly inhomogenous systems: a mathematical basis for the synthesis of higher gradients metamaterials. *Arch. Ration. Mech. Anal.* **218**, 1239–1262. (doi:10.1007/s00205-015-0879-5)

[26] Pideri C, Seppecher P. 1997 A second gradient material resulting from the homogenization of an heterogeneous linear elastic medium. *Contin. Mech. Thermodyn.* **9**, 241–257. (doi:10.1007/s001610050069)

[27] Javili A, dell'Isola F, and Steinmann P. 2013 Geometrically nonlinear higher-gradient elasticity with energetic boundaries. *J. Mech. Phys. Solids*, **61**(12), 2381–2401. (doi:10.1016/j.jmps.2013.06.005)

[28] Bertram A. 2015 Finite gradient elasticity and plasticity: A constitutive mechanical framework. *Continuum Mech. Thermodyn.*, **27**(6), 1039–1058. (doi:10.1007/s00161-015-0417-6)

[29] Melnik AV, and Goriely A. 2013 Dynamic fiber reorientation in a fiber-reinforced hyperelastic material. *Math. Mech. Solids* **18**, 634–648. (doi:10.1177/1081286513485773)

[30] Grillo A, Wittum G, Tomic A, Federico S. 2015 Remodelling in Statistically Oriented Fibre-Reinforced Composites and Biological Tissues. *Math. Mech. Solids* **20**, 1107–1129. (doi:10.1177/1081286513515265)

[31] Goda I, Assidi M, Ganghoffer JF. 2014 A 3D elastic micropolar model of vertebral trabecular bone from lattice homogenization of the bone microstructure. *Biomech. Model. Mechanobiol.* **13**, 53–83. (doi:10.1007/s10237-013-0486-z)

[32] Lekszycki T, dell'Isola F. 2012 A mixture model with evolving mass densities for describing synthesis and resorption phenomena in bones reconstructed with bio-resorbable materials. *Z. Angew. Math. Mech.* **92**, 426–444. (doi:10.1002/zamm.201100082)

[33] Maugin, G. A. 2011 Solitons in elastic solids (1938–2010). *Mech. Res. Commun.*, **38**(5), 341–349. (doi: 10.1016/j.mechrescom.2011.04.009)

[34] Cohen H. 1966 A non-linear theory of elastic directed curves. *Int. J. Engng Sci.*, **4**, 511–524. (doi:10.1016/0020-7225(66)90013-9)

[35] Green AE, Laws N. 1966 A General Theory of Rods, *Proc. R. Soc. Lond. A*, **293**, 145–155 (doi:10.1098/rspa.1966.0163)

[36] Naghdi PM. 1981 Finite Deformation of Elastic Rods and Shells. In: Carlson D.E., Shield R.T. (eds) *Proceedings of the IUTAM Symposium on Finite Elasticity.* Springer, Dordrecht. (doi:10.1007/978-94-009-7538-5_4)

[37] Antman SS. 1973 The Theory of Rods. In: Truesdell C. (eds) Linear Theories of Elasticity and Thermoelasticity. Springer, Berlin, Heidelberg. (doi:10.1007/978-3-662-39776-3_6)

[38] Steigmann DJ, Faulkner MG. 1993 Variational theory for spatial rods, *J Elasticity*, **33**: 1–26. (doi:10.1007/BF00042633)

[39] Pietraszkiewicz W., Eremeyev VA. 2009 On natural strain measures of the non-linear micropolar continuum, *Int. J. Solids Struct.*, **46**, Issue 3, 774–787, (doi:10.1016/j.ijsolstr.2008.09.027)

[40] Altenbach H, Eremeyev VA, Lebedev LP. 2011 Micropolar Shells as Two-dimensional Generalized Continua Models. In: Altenbach H., Maugin G., Erofeev V. (eds) Mechanics of Generalized Continua. Advanced Structured Materials, vol 7. Springer, Berlin, Heidelberg (doi:10.1007/978-3-642-19219-7_2)

[41] dell'Isola F, Maier G, Perego U, Andreaus U, Esposito R, Forest S. 2014 The complete works of Gabrio Piola: Volume I - Commented English Translation. *Adv. Struct. Mater.* **38**, 1–813. (doi:10.1007/978-3-319-00263-7)

[42] Placidi L, Barchiesi E, Della Corte A. (2017) Identification of Two-Dimensional Pantographic Structures with a Linear D4 Orthotropic Second Gradient Elastic Model Accounting for External Bulk Double Forces. In: dell'Isola F., Sofonea M., Steigmann D. (eds) *Mathematical Modelling in Solid Mechanics*. Advanced Structured Materials, vol **69**, 211–232. Springer, Singapore. (doi:10.1007/978-981-10-3764-1_14)

[43] Placidi L, Andreaus U, Della Corte A, Lekszycki T. 2015 Gedanken experiments for the determination of two-dimensional linear second gradient elasticity coefficients. *Z. Angew. Math. Phys.* **66**, 3699–3725. (doi:10.1007/s00033-015-0588-9)

[44] Dietrich L, Lekszycki T, Turski K. 1998 Problems of identification of mechanical characteristics of viscoelastic composites. *Acta Mech.* **126**, 153–167. (doi:10.1007/BF01172805)

[45] Fischer P, Klassen M, Mergheim J, Steinmann P, Müller R. 2011 Isogeometric analysis of 2D gradient elasticity. *Comput. Mech.* **47**, 325–334. (doi:10.1007/s00466-010-0543-8)

[46] Greco L, Cuomo M. 2014 An implicit G1 multi patch B-spline interpolation for Kirchhoff–Love space rod. *Comput. Methods Appl. Mech. Eng.* **269**, 173–197. (doi:10.1016/j.cma.2013.09.018)

[47] Greco L, Cuomo M, Contrafatto L, Gazzo S. 2017 An efficient blended mixed B-spline formulation for removing membrane locking in plane curved Kirchhoff rods. *Comput. Methods Appl. Mech. Eng.*, **324**: 476–511. (doi:10.1016/j.cma.2017.06.032)

[48] Wang CM, Zhang H, Gao RP, Duan WH, Challamel N. 2015 Hencky Bar-Chain Model for Buckling and Vibration of Beams with Elastic End Restraints. *Int. J. Str. Stab. Dyn.* **15**, 1540007. (doi:10.1142/S0219455415400076)

[49] Kocsis A, Challamel N, Károlyi G. 2017 Discrete and nonlocal models of Engesser and Haringx elastica, *Int. J. Mech. Sci.*, **130**, 571–585. (doi:10.1016/j.ijmecsci.2017.05.037)

[50] Turco E, dell'Isola F, Cazzani A, Rizzi NL. 2016 Hencky-type discrete model for pantographic structures: numerical comparison with second gradient continuum models, *Z. Angew. Math. Phys.*, **67** (4), August 2016 (First online: 25 June 2016), 28 pages. (doi:10.1007/s00033-016-0681-8).

[51] Forest S, Sievert R. 2006 Nonlinear microstrain theories. *Int. J. Solids Struct.* **43**, 7224–7245. (doi:10.1016/j.ijsolstr.2006.05.012)

[52] Yang Y, Misra A. 2010 Higher-order stress–strain theory for damage modeling implemented in an element-free Galerkin formulation. *Comput. Model. Engng. Sci.*, **64**, 1–36. (doi:10.3970/cmes.2010.064.001)

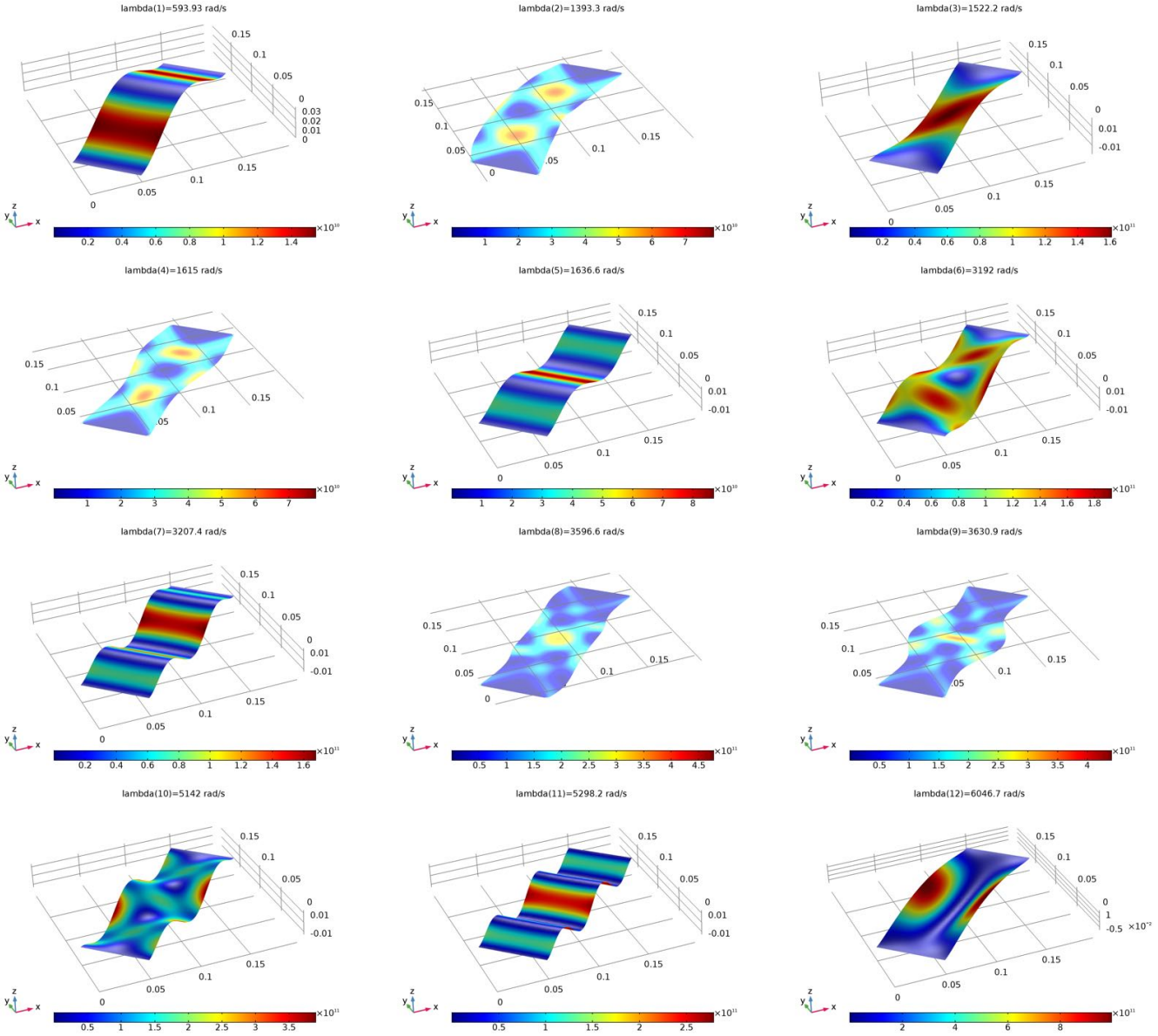

Figure 9: Mode shapes for reference configuration. Strain Energy

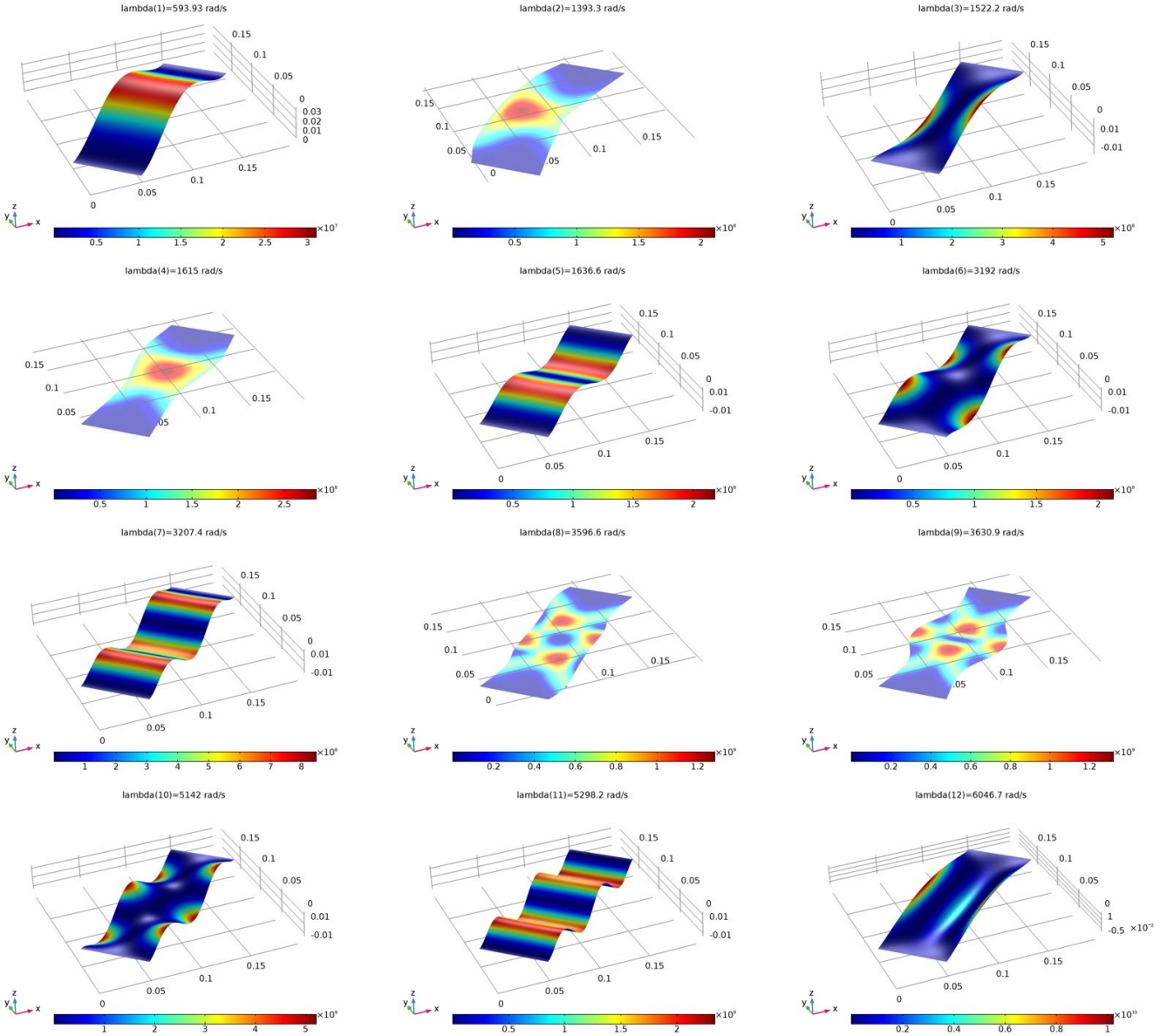

Figure 10: Mode shapes for reference configuration. Kinetic Energy

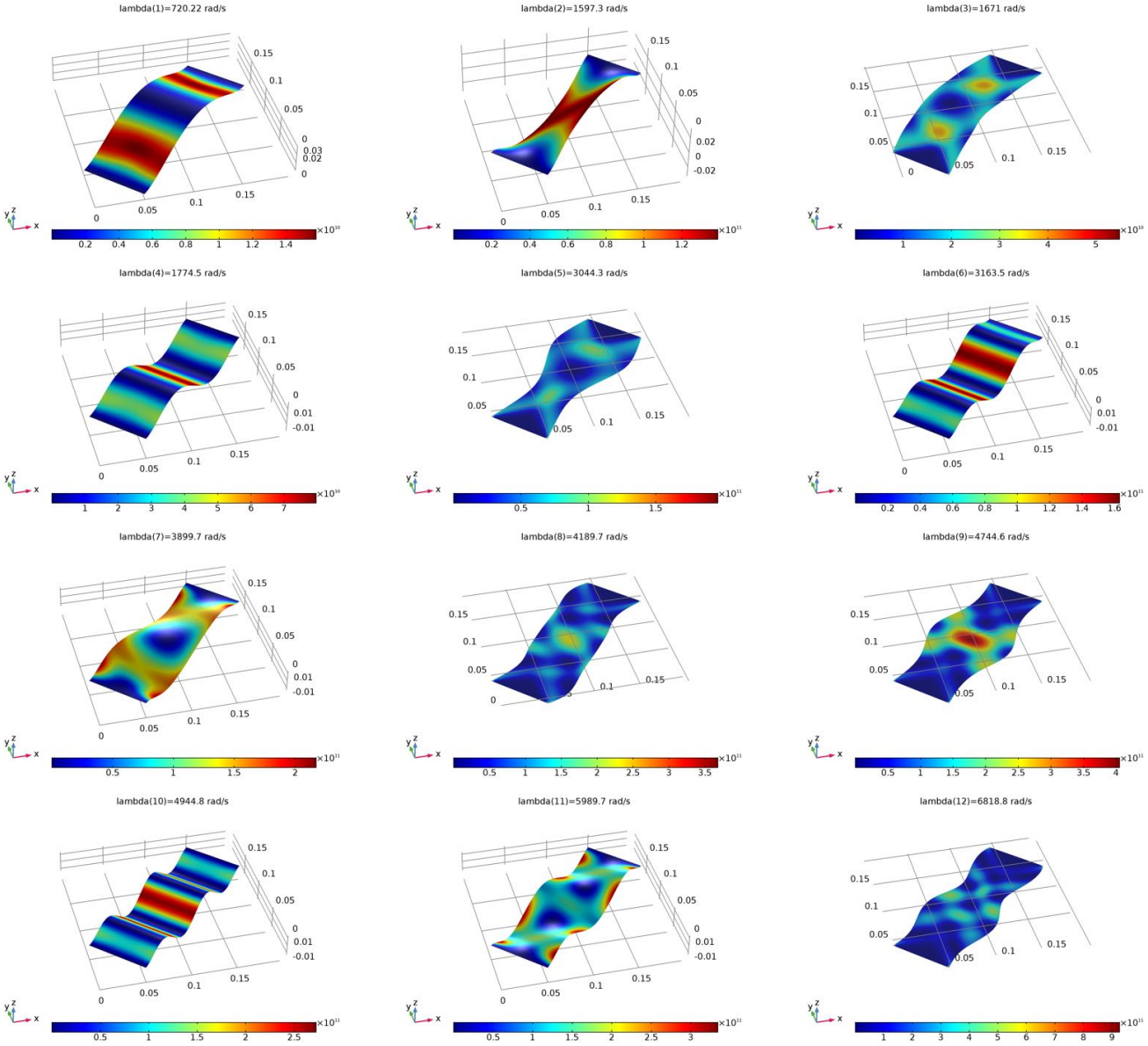

Figure 11: Mode shapes for pre-stretched configuration. Strain Energy

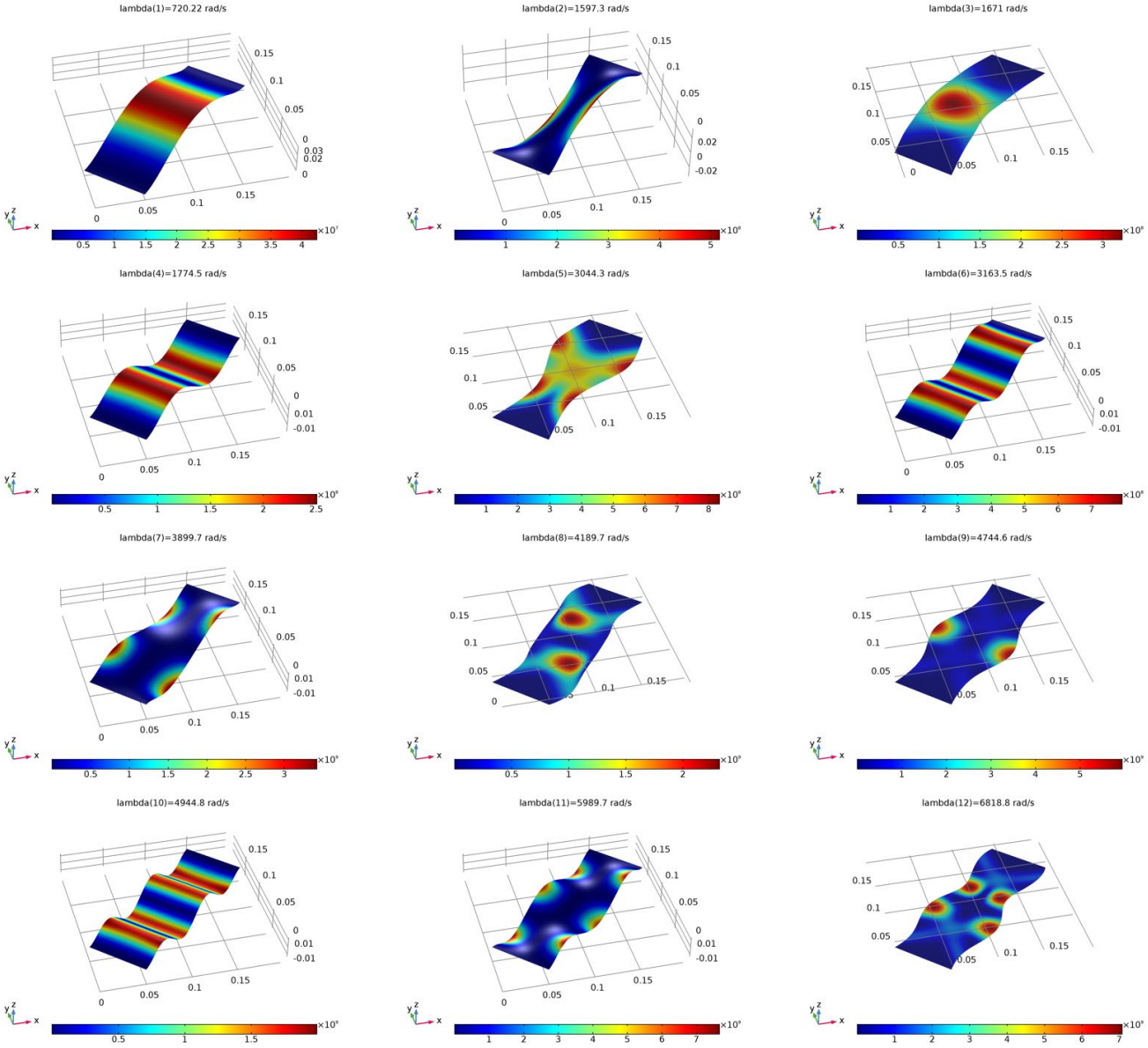

Figure 12: Mode shapes for pre-stretched configuration. Kinetic Energy